Heliyon 9 (2023) e22512

Contents lists available at ScienceDirect

Heliyon

journal homepage: www.cell.com/heliyon

Bi_2O_2Se-based CBRAM integrated artificial synapse

Dharmendra Verma [a], Tsung-Cheng Chen [a], Bo Liu [b], Chao-Sung Lai [a,c,d,*]

[a] Department of Electronic Engineering, Chang Gung University, Taoyuan 33302, Taiwan
[b] Faculty of Information Technology, College of Microelectronics, Beijing University of Technology, Beijing 100124, People's Republic of China
[c] Department of Nephrology, Chang Gung Memorial Hospital, Linkou 33302, Taiwan
[d] Department of Materials Engineering, Ming-Chi University of Technology, New Taipei City 24301, Taiwan

ARTICLE INFO

Keywords:
2D material
Bi_2O_2Se
Cross point structure
CBRAM
Artificial synapse

ABSTRACT

Integrating two-dimensional (2D) semiconducting materials into memristor structures has paved the way for emerging 2D materials to be employed in a vast field of memory applications. Bismuth oxyselenide (Bi_2O_2Se), a 2D material with high electron mobility, has attracted significant research interest owing to its great potential in various fields of advanced applications. Here, we explore the out-of-plane intrinsic switching behavior of few-layered Bi_2O_2Se via a cross point device for application in conductive bridge random access memory (CBRAM) and artificial synapses for neuromorphic computing. Via state-of-the-art methods, CVD-grown Bi_2O_2Se nanoplate is applied as a switching material (SM) in an Al/Cu/Bi_2O_2Se/Pd CBRAM structure. The device exhibits ~90 consecutive DC cycles with a tight distribution of the SET/RESET voltages under a compliance current (CC) of 1 mA, a retention of over 10 ks, and multilevel switching characteristics showing four distinct states at Vread values of 0.1, 0.2, 0.25, and 0.3 V. Moreover, an artificial synapse is realized with potentiation and depression by modulating the conductance. The switching mechanism is explained via Cu migration through Bi_2O_2Se based on HRTEM analysis. The present structure shows potential for future integrated memory applications.

1. Introduction

In parallel with the Internet of Things (IoT) and artificial intelligence (AI), devices with a high storage capacity for ease of storage, computing, and transmission are becoming more crucial to deal with the excessive information [1]. The traditional von Neumann architecture based on physically separated memory and processors adds challenges for the processing speed and energy-efficient data transfer due to bottleneck. Among various technological developments, complementary metal–oxide–semiconductor (CMOS) technology is widely accepted because of its merits, including being favorable in the semiconductor industry in terms of design and fabrication within scaling limits following Moore's law [2]. The scaling restriction with CMOS technology has revolutionized various emerging memory techniques during the last couple of decades. Foremost are magnetic random access memory (MRAM), phase change memory (PCM), ferroelectric random access memory (FERAM), and resistive random access memory (RRAM) [3,4]. Among them, RRAM is well considered to be the most capable for future data storage technology because of its merits of smaller storage cells, a higher storage density, and faster speeds in write and read processes [5–9].

The fundamental configuration of RRAM is based on a metal–insulator–metal (MIM) structure with a top electrode (TE) and a bottom electrode (BE) separated by at least one dielectric layer or a switching material (SM) [10]. The key parameters (reported with

* Corresponding author.Department of Electronic Engineering, Chang-Gung University, Taoyuan, 33302, Taiwan.
E-mail address: cslai@mail.cgu.edu.tw (C.-S. Lai).

https://doi.org/10.1016/j.heliyon.2023.e22512
Received 31 May 2023; Received in revised form 30 October 2023; Accepted 14 November 2023
Available online 17 November 2023

critical values) for RRAM are as follows: (1) resistance ratio: ratio of the resistances in the HRS and LRS, 10^9; (2) endurance: maximum number of recoverable cycles between the HRS and LRS, 10^{12}; (3) retention: time duration for data storage, 10 years; (4) operating voltage: minimum voltage required to alter the resistance states from the LRS to the HRS or from the HRS to the LRS; and (5) switching speed: write voltage pulse width, 10 ns [11–13]. The switching behavior of RRAM devices has been extensively studied, with their further classification into two major categories, namely, valence change memristors (VCMs) and electrochemical metallization memristors (ECMs). The switching mechanism in VCMs critically depends on ion vacancies or oxygen vacancies in the SM. Although VCMs are fascinating for their well-suited process and steady switching characteristics, they face challenges of a lower dynamic range, a higher off current (excess power feeding), and uncontrolled ion movement. Conductive-bridge random access memories (CBRAMs), also known as ECMs, employ switching behavior based on the formation of conductive filaments between the TE and BE via the redox reaction of the metal. Overcoming the demerits of VCMs, CBRAMs are widely considered to have a higher dynamic range, a lower off current (higher on-off ratio), a higher switching speed, and upgraded scalability [14–16]. CBRAM, in its primitive structure, comprises a specific switching material (SM) sandwiched between an electrochemically active metal electrode (Cu, Ag) and an electrochemically inert metal electrode (W, Pt, TiN) [17]. For the switching materials in CBRAM, different classes of materials have been explored, including chalcogenide glasses [18], oxides [19], polymers [20], g-C_3N_4 and its nanocomposites [21,22]. All these existing SMs have scalability challenges.

Two-dimensional materials (2DMs), such as MoS_2 [23,24], h-BN [25], black phosphorus [26], and MXene [27], have been investigated as SMs and electrodes for CBRAM applications. Because of the layered structure containing atomically thin layers, 2DMs facilitate low voltage operation and stable resistive switching characteristics. Since the implementation of 2DMs in CBRAM results in an improvement in performance, exploring new 2DMs for CBRAM remains an open and important research area for realizing CBRAM with optimum performance.

Recently, the atomically thin ternary 2DM bismuth oxyselenide (Bi_2O_2Se), with a suitable bandgap, has received much attention due to its quasi-2D structure, high electron mobility, and robust air stability [28–30]. Bi_2O_2Se presents a highly symmetric atomic structure with a tetragonal lattice (*I4/mmm*; a = b = 3.88 Å, c = 12.16 Å) where eight Bi atoms compose a cube with a Se atom at the body center and with uniform alignment of $[Bi_2O_2]_n^{2n+}$ layers along the c axis. With a key difference from van der Waals layered 2DMs, Bi_2O_2Se is recognized as an ionic layered material formed via cation, $[Bi_2O_2]_n^{2n+}$, and anion, $[Se]_n^{2n-}$, stacked layers through weak electrostatic interactions. However, similar to other 2DMs, Bi_2O_2Se shows characteristics of layer-number dependent bandgap and optical absorption [31]. Bi_2O_2Se has a low electron effective mass of $\sim 0.14m_0$, which is lower than that of silicon ($\sim 0.26m_0$) and MoS_2 ($\sim 0.4m_0$), revealing a high electron mobility suitable for electronic and optoelectronic applications [32–34]. Wu et al. reported that the electron Hall mobility of a nonencapsulated Bi_2O_2Se flake (~20.9 nm) was measured to be 28,900 and 150 $cm^2 V^{-1} s^{-1}$ at 1.9 K and room temperature, respectively [28]. The synthesis of Bi_2O_2Se is one of the key interests of this research. Different approaches have been reported for the synthesis of Bi_2O_2Se, including hydrothermal [35,36], solution-assisted [37], composite-molten-salt (CMS) [38], and vapor deposition processes [28,31]. Wu et al. demonstrated the synthesis of 2D Bi_2O_2Se single crystals (grain size ~ 200 μm, thickness down to monolayer ~ 0.61 nm) on mica substrates via coevaporation of Bi_2O_3 and Bi_2Se_3 powders as precursors by the chemical vapor deposition (CVD) method. In the CVD approach for the synthesis of Bi_2O_2Se, a mica substrate is widely used because the strong Coulomb interaction between mica and Bi_2O_2Se facilitates the lateral growth of Bi_2O_2Se for large-scale 2D Bi_2O_2Se sheets [31]. Recently, Khan et al. reported the synthesis of a 2D Bi_2O_2Se single crystal with a grain size on the order of millimeters and thickness down to a monolayer by an ambient-pressure vapor–solid (VS) deposition approach [39]. The unique structural and physical properties of Bi_2O_2Se have been further proven by implementation in devices for novel applications such as thin film transistors [40,41], photodetectors [42,43], artificial synapses [44,45], multifunctional optoelectronics [46], and optical switches [47]. Recently, Bi_2O_2Se has been employed in memristor structures [44]. As an example, Liu et al. demonstrated a Bi_2O_2Se-based memristor (three terminals) via the application of Bi_2O_2Se nanoplates as the bottom electrode (BE). With aid of the similar structure, the function of the "NAND" gate was realized by tuning the electric field polarity of Bi_2O_2Se through a metal contact (Pd) [48]. In another study, Chen et al. demonstrated out-of-plane resistive switching of thick Bi_2O_2Se flakes by forming hillocks via the application of a vertical electric field [49]. Recently, Liu et al. extended the application of the Bi_2O_2Se-based memristor (three terminal) structure to security applications by employing the device as a true random number generator [50]. Moreover, Lai et al. reported advanced impacts of nanotechnology, including recent Bi_2O_2Se-based miscellaneous reports [51]. Although many reports have demonstrated significant efforts for the application of Bi_2O_2Se in memristors, the implementation of Bi_2O_2Se as a true SM in memristors remains elusive.

Motivated by recent reports on the application of Bi_2O_2Se in memristor devices, here, we explore the inherent intrinsic switching property of Bi_2O_2Se by implementing it as an SM in the CBRAM structure Al/Cu/Bi_2O_2Se(SM)/Pd/SiO_2/Si. The fabricated device exhibits basic switching characteristics at low voltage levels <1.5 V, including endurance (~90 cycles), cumulative probability (~99 %), and retention @ Vread of 0.1 V for over 10 ks. With the aid of distinct Vread values of 0.1 V, 0.2 V, 0.25 V and 0.3 V, multilevel switching characteristics are realized. Moreover, artificial synapses are realized by means of potentiation (35 states) and depression (41 states). The switching mechanism is proposed to occur via migration of Cu ions through SM Bi_2O_2Se based on HRTEM analysis. Therefore, the presented results show sufficient potential for Bi_2O_2Se-based CBRAM for future advanced memory applications enriched with artificial neuromorphic activities.

2. Experimental section

2.1. Synthesis of Bi_2O_2Se nanoplates on a mica substrate

Two-dimensional highly crystalline single-grain Bi_2O_2Se nanoplates were first synthesized by using the low-pressure chemical

vapor deposition (LPCVD) technique [45]. Bismuth oxide (Bi_2O_3) and bismuth selenide (Bi_2Se_3) were used as the precursors placed upstream of the tube. Mica was used as the substrate since it supports uniform lateral growth of Bi_2O_2Se nanoplates due to the strong interaction between mica and Bi_2O_2Se [45]. The substrate was placed downstream of the tube. Ar (200 sccm) was used as the carrier gas under emblematic growth conditions of 700 °C for 40 min with a tube pressure of 100 Torr.

2.2. Material characterization

The Raman spectrum for Bi_2O_2Se was measured via a 532 nm laser with a 100x objective lens (UniDRON, CI Technology). Atomic force microscopy (AFM B067, Bruker Corp.) was carried out to determine the thickness of the developed Bi_2O_2Se nanoplates. A microscope system (OLYMPUS BX53 M) was used to obtain OM images of the fabricated Bi_2O_2Se-based device. The elemental composition was confirmed by X-ray photoelectron spectroscopy (XPS) survey (ULVAC-PHI, INC) analysis.

2.3. Device fabrication

As-synthesized Bi_2O_2Se nanoplates were transferred from the mica substrate onto a palladium (Pd) electrode via PMMA, water, and OM assisted method (details in S1 and S2). This Pd electrode was the bottom electrode (BE) for Bi_2O_2Se-based CBRAM. The pattern for the top electrode (TE) was made by an LED lithography system by defining the Bi_2O_2Se area to be sandwiched as the switching material (SM) between the TE and BE. For TE, Al/Cu metals (60 nm/40 nm) were deposited by a thermal evaporator. Liftoff yielded the two-terminal cross point Bi_2O_2Se-based CBRAM structure.

2.4. Measurements

For electrical measurements of the CBRAM device, B1500A semiconductor device analyzer was used. All measurements were completed in a closed environment at room temperature.

3. Results & discussion

Fig. 1a shows a schematic diagram of the layered crystal structure of Bi_2O_2Se with integral elements "Bi", "O", and "Se" in distinguishable colors green, red, and blue, respectively. The schematic integrates four layers of cation $[Bi_2O_2]_n^{2n+}$, and anion $[Se]_n^{2n-}$, interacting electrostatically in concept [31]. Fig. 1b shows an atomic force microscopy (AFM) image of an as-grown Bi_2O_2Se nanoplate on a mica substrate. The thickness of the selected Bi_2O_2Se nanoplate is observed to be ~25 nm (~42 layers: monolayer thickness =

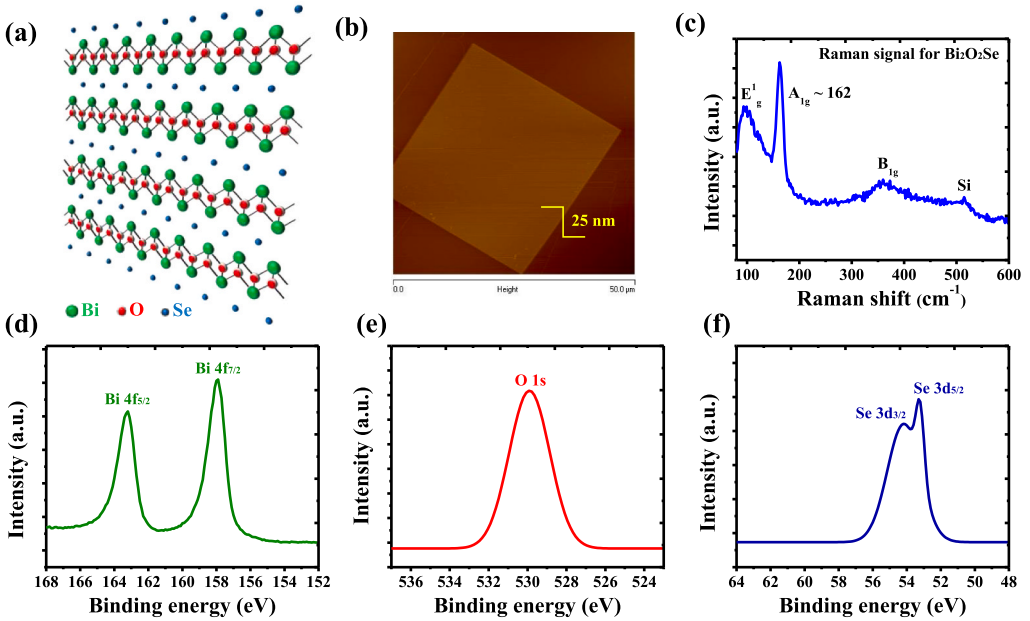

Fig. 1. Material characterization of a synthesized Bi_2O_2Se nanoplate. (a) Schematic view of the layered structure composed of the constituent atoms "Bi" (green), "O" (red), and "Se" (blue). (b) AFM image of a Bi_2O_2Se single nanoplate of thickness ~ 25 nm. (c) Raman signal for Bi_2O_2Se transferred onto a Si substrate presenting main peak A_{1g} at 162 cm^{-1}. XPS spectrum of the Bi_2O_2Se nanoplate (d). The peaks for Bi are located at 163.2 eV and 157.9 eV, corresponding to the binding energies of Bi $4f_{5/2}$ and Bi $4f_{7/2}$, respectively. (e) The peak for O1s is located at 529.9 eV, representing oxygen associated with the crystal lattice. (f) XPS spectrum of Se showing two peaks at 54.2 eV and 53.3 eV, relating to the binding energies of Se $3d_{3/2}$ and Se $3d_{5/2}$, respectively.

0.608 nm) [31], with lateral dimensions of ~40 μm on all sides showing a square shape. The dimensions of the Bi_2O_2Se nanoplate are found to be sufficient for its implementation in the device. Fig. 1c shows the Raman analysis of the transferred Bi_2O_2Se nanoplate. The distinctive peak A_{1g} appears at 162 cm^{-1}, evidencing the successful synthesis and transfer process (the detailed transfer process is given in the experimental section). The Raman signal also contains other characteristic peaks at ~95, 355, and 520 cm^{-1} corresponding to E_g^1 (for α-Bi_2O_3), B_{1g} (for out-of-plane vibrations of "O" atoms), and Si (substrate), respectively [30]. X-ray photoelectron spectroscopy (XPS) was performed to analyze the chemical bonding states of the constituent elements of Bi_2O_2Se, as shown in Fig. 1d-e-f. As observed, the peaks for Bi are located at approximately 163.2 eV and 157.9 eV, relating to the binding energies of Bi $4f_{5/2}$ and Bi $4f_{7/2}$, respectively. The peak for O1s is observed at 529.9 eV, corresponding to the oxygen associated with the crystal lattice. The dual-peak resolved spectrum of Se shows peaks at 54.2 eV and 53.3 eV, relating to the binding energies of Se $3d_{3/2}$ and Se $3d_{5/2}$, respectively. The XPS analysis confirms the synthesized Bi_2O_2Se nanoplates are in adequate elemental quality.

3.1. Resistive switching characteristics

The fabricated Bi_2O_2Se-based CBRAM device was first utilized to demonstrate basic bipolar resistive switching characteristics. Fig. 2a presents the first DC sweep cycle (as measured) with a compliance current (CC) of 1 mA. For the first cycle, the device attains the CC at a sweep voltage of 1.3 V, showing a forming voltage (Vform) of 1.3 V (formation of conductive path between TE and BE through SM), and the RESET voltage for the first cycle is −1 V (rupturing of conductive path formed between TE and BE).

The direction of the current with respect to the sweep voltage is indicated by the arrow.

Fig. 2b presents 90 consecutive DC sweep I–V cycles. The SET voltage (Vset) distribution is from 0.6 to 0.8 V (excluding the first cycle), and the RESET voltage (Vreset) distribution is from −0.4 to −1.4 V. In addition, the voltage values for the SET and RESET conditions are presented via the cumulative probability distribution shown in Fig. S3. The plot displays more variation in Vreset than in Vset. Furthermore, a statistical analysis of the switching voltages under the SET and RESET conditions was performed.

The calculated numerical values of the mean, standard deviation, and coefficient of variation (%) are 0.66, 0.09 and 14 for Vset and 0.61, 0.26, and 43 for Vreset (mode), respectively, as presented in Table-ST1.

The endurance plot of DC cycles for the HRS (red color)/LRS (green color) @ Vread ~ 0.1 V shows in spite of significant variation in HRS values, the separation between the HRS and LRS is higher than 10 (Fig. 2c). We believe that the possible reason for lower HRS/LRS ratio is because of conductive nature of Bi_2O_2Se which needs further study for more exploration. The cycle-to-cycle cumulative probability for the HRS and LRS is presented in Fig. 2d which further confirms that HRS and LRS values are separated by least value 10. Next, the device was measured for the retention characteristics. Fig. 2e shows retention in the HRS and LRS measured at Vread ~0.1 V with slight deterioration in HRS, and the differentiation between the two states is significantly maintained for over 10 ks. For the HRS, the resistance values at 1 s and 10 ks are measured to be ~14.15 kΩ and ~13.18 kΩ, respectively, while for the LRS, the resistance

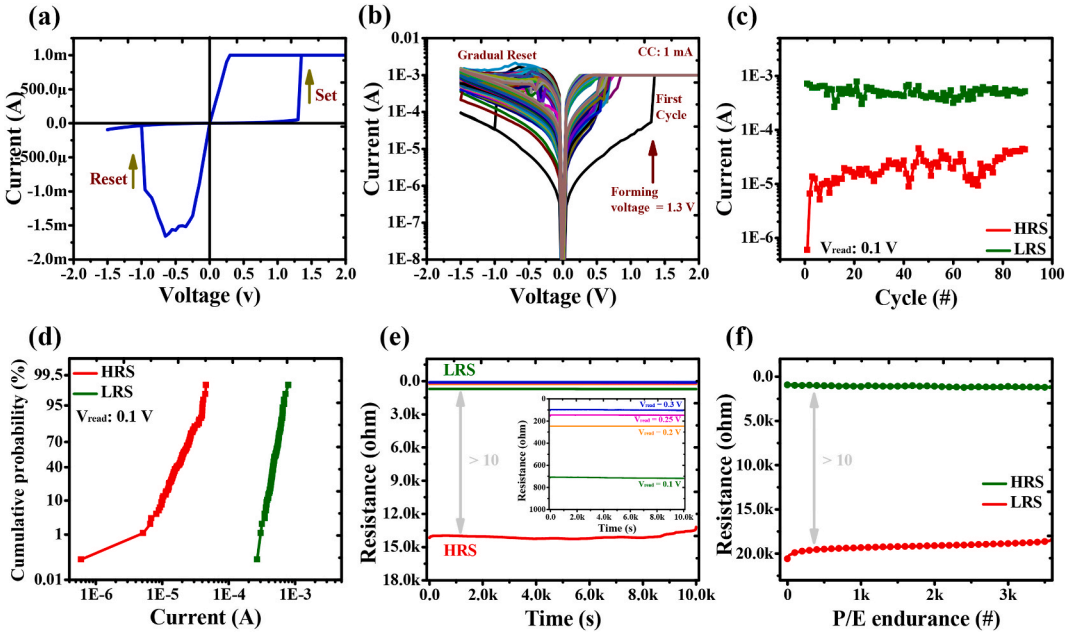

Fig. 2. Switching characteristics of Bi_2O_2Se-based CBRAM. (a) Voltage sweep for the first cycle (set ~ 1.3 V, reset ~ −1 V) as measured with a CC of 1 mA. (b) I–V curves for 90 DC sweep cycles @ a CC of 1 mA. (c) Endurance plot for the HRS/LRS @ a Vread of 0.1 V. (d) Cumulative distribution of the HRS/LRS in DC sweep cycles. (e) Retention characteristics of switching in the HRS/LRS for 10 ks with a multilevel switching property (observed in the LRS) showing four different switching levels at Vread values of 0.1 V, 0.2 V, 0.25 V and 0.3 V. (f) P/E endurance characteristics with an applied pulse width of 100 ns.

values at 1 s and 10 ks are measured to be ~706 Ω and ~718 Ω, respectively, with both states HRS/LRS showing ratio R_{HRS}/R_{LRS} >10. To explore multilevel switching characteristics, different values of Vread were applied to the device in the LRS. Four distinct switching levels are observed by applying Vread = 0.1, 0.2, 0.25, and 0.3 V, as depicted in Fig. 2e. At time t = 1 s, the LRS levels for Vread = 0.1, 0.2, 0.25, and 0.3 V are measured to be 706, 245, 145, and 97 Ω, respectively, while at t = 10 ks, the LRS levels for Vread = 0.1, 0.2, 0.25, and 0.3 V are measured to be 718, 245, 147, and 102 Ω, respectively. The four different switching states are quite stable and separated from each other through a time span of 10 ks, proving the device capability to exhibit multilevel resistive switching characteristics. Fig. 2f represents a quite consistent P/E endurance of 3.6 K cycles under voltage pulse (1 V/−0.8 V) application with a pulse width of 100 ns.

3.2. Current conduction mechanism

To deeply understand the current conduction mechanism of the Bi_2O_2Se-based CBRAM device, the 7th I–V characteristic curve (out of the 90 presented in Fig. 2b) was randomly selected, which showed HRS and LRS regions, as presented in Fig. 3a. Fig. 3b presents a replot (generated by taking 10 points from 2 to 11 as measured data) of the HRS current under a positive bias in $\ln(J/T^2)$ versus $\sqrt{E}$ form (where J is the current density.

T is the absolute temperature, and E is the electric field), which shows that the HRS includes Schottky conduction. To determine the dynamic dielectric constant (Ɛsch) and Schottky barrier height (φ_B), the following equations were used [52].

$$Slope = \left(\sqrt{\frac{q^3}{4\pi\varepsilon_o\varepsilon_{sch}(k_BT)^2}}\right) \tag{1}$$

$$Intercept = \frac{q\varnothing_B}{k_BT} \tag{2}$$

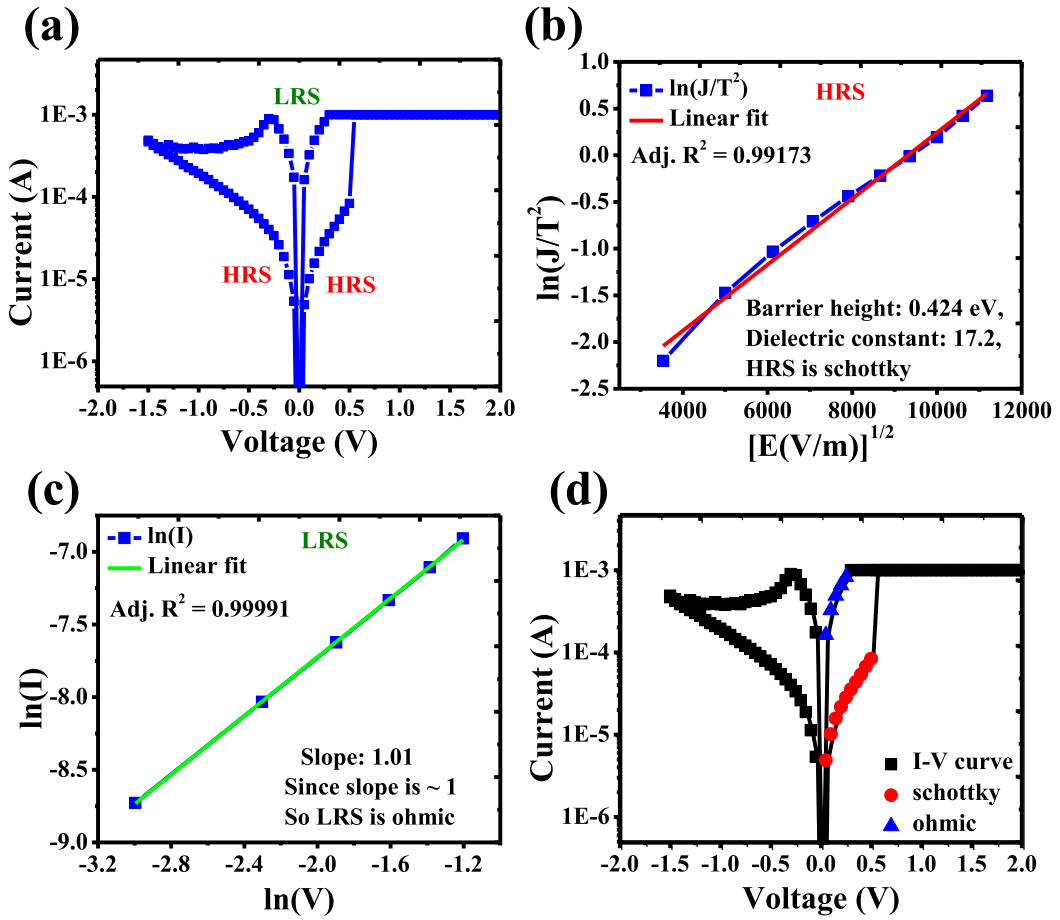

Fig. 3. Analysis of the current conduction mechanism. (a) Typical I–V characteristics of the 7th cycle out of 90 DC sweep cycles with a CC of 1 mA showing the HRS and LRS. (b) Fitting curve for Schottky conduction in the HRS under a positive bias. (c) Fitting curve for Ohmic conduction in the LRS under a positive bias. (d) Fully fitted I–V curve discriminating Schottky and Ohmic conduction regions.

in Equations (1) and (2), q, ε_o, and k_B represent the electronic charge, permittivity of free space, and Boltzmann's constant, respectively. From the slope and intercept, the calculated values of εsch and φ_B are 17.2 and 0.424 eV, respectively. The dielectric constant is high, which is consistent with previous reports for oxygen-rich Bi_2O_2Se [49]. Fig. 3c presents the replot of the LRS generated by taking 6 consecutive points in ln(I) versus ln(V) form, and the measured value of the slope is ~1.01. Since the slope is ~1, the LRS conduction is Ohmic conduction. In linear fitting the Adj. R^2 values for HRS (Fig. 3b) and LRS (Fig. 3c) are 0.99173 and 0.99991 respectively. Both Schottky (red points) and Ohmic (blue points) conductance regions are clearly revealed in the fully fitted I–V (black) curve, as shown in Fig. 3d.

3.3. Artificial synapse characteristics

Apart from data storage, memory devices have been explored for mimicking other functions that includes synapses [21], and nociceptors [53]. The present device was further utilized to mimic basic neuromorphic characteristics such as potentiation and depression. Positive and negative DC sweep voltages were applied to realize potentiation and depression. Fig. 4a shows the potentiation characteristics. For potentiation, a constant positive DC sweep voltage (0 → 0.3 V) was uninterruptedly applied. The device shows a moderate current increment almost in a linear fashion representing 35 distinct current levels from ~20 μA (first level due to the first + ve DC sweep) to ~ 160 μA (35th level in response to the 35th + ve DC sweep), indicating that the average current increment per DC sweep is ~4 μA.

In principle, the potentiation exhibits a partial SET condition via the gradual formation of CFs by applying a positive voltage in precisely controlled steps, and hence, the current also gradually increases.

Fig. 4b presents depression characteristics. For depression, a fixed negative DC sweep voltage (0 → −0.6 V) was uninterruptedly applied. The device shows a moderate current decrement representing 41 distinct current levels from ~320 μA (first level due to the first -ve DC sweep) to ~ 75 μA (41st level in response to the 41st -ve DC sweep), indicating that the average current decrement per DC sweep is ~6 μA. Conceptually, depression is tuning the device to the RESET condition via gradual rupturing of the formed CFs by applying a negative voltage in precisely controlled steps, leading to a gradual decrease in the current. For clear visualization of potentiation/depression phenomena, measured values were extracted and replotted as the conductance versus number of DC sweeps, as shown in Fig. 4c. It is clear that the device conductance gradually increases during potentiation and then gradually decreases during depression. Precisely controlled voltage pulses with a pulse duration of 100 ns were applied to obtain LTP (0.3 V) and LTD (−0.6 V)

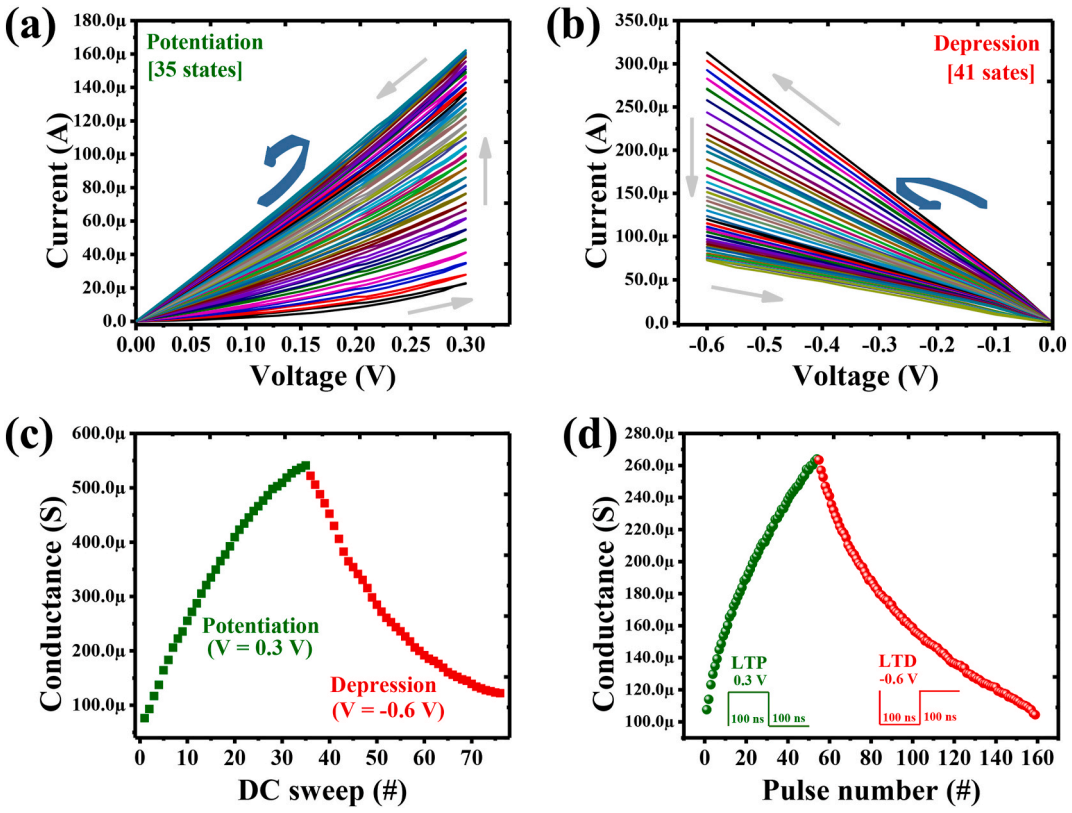

Fig. 4. Mimicking artificial synapse via conductivity modulation. (a) potentiation: 35 states. (b) depression: 41 states. (c) added conductance values for potentiation and depression versus number of DC sweeps. (d) Voltage pulse modulated LTP/LTD characteristics.

characteristics presented by the device, as shown in Fig. 4d.

3.4. Proposed mechanism for resistive switching and artificial synapses

The proposed switching mechanism is based on the migration of Cu ions through SM Bi_2O_2Se under an appropriate external bias, as schematically explained in Fig. 5. Fig. 5-a presents the Bi_2O_2Se-based CBRAM structure in its primitive state. Fig. 5-b shows that the device is tuned to the SET condition by applying a positive voltage sweep on the TE. Under the SET condition, excess Cu ions are generated due to the formation of CuOx (x = 1,2) at the Cu/Bi_2O_2Se interface at the time of Cu deposition on Bi_2O_2Se following $Cu^0 \rightarrow Cu^{z+} + ze^-$ (z = 1 or 2). These Cu ions migrate through layered Bi_2O_2Se, forming a conductive path (or a conductive filament - CF). Reduction of these Cu ions is expected at the Bi_2O_2Se/PdOx interface due to tunneling of electrons from the bottom electrode (BE) Pd through PdOx. PdOx shows less oxygen, indicating metallic-like properties. The work function of PdOx is 4.8 eV, and that of Pd is 4.95 (±0.05) eV. Since the work function difference between PdOx/Pd is low, Ohmic contact facilitates a number of electrons passing through PdOx and reducing the Cu^{z+} ions to Cu^0. The thicker switching layer of Bi_2O_2Se (~25 nm) can control the migration of Cu ions through it; therefore, the formation of multiple weak CFs can be expected. Additionally, the crystalline nature of Bi_2O_2Se can be another potential barrier to Cu ion migration. Fig. 5-c elucidates the RESET process (by applying a negative voltage sweep at the TE),

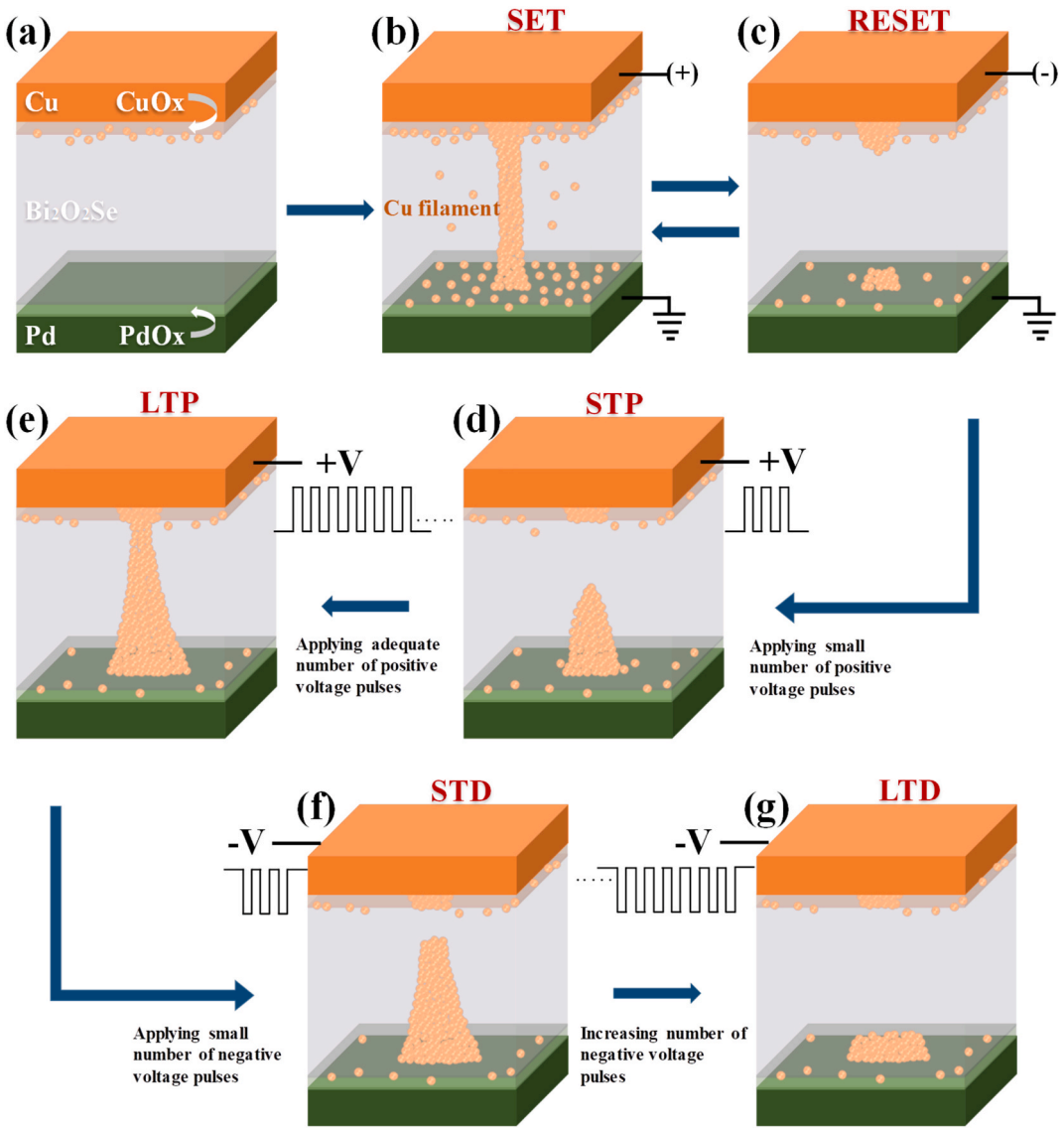

Fig. 5. Schematic representation of the switching mechanism. (a) Primitive view of the device structure. (b) Device under SET and (c) RESET conditions. (d) STP via formation of smaller CFs by applying a few positive voltage pulses. (e) Strengthening of CFs leading to LTP upon application of pulses in large numbers. (f–g) Weakening of CFs by applying negative voltage pulses in small and large numbers for STD and LTD, respectively.

and the flow of I_{RESET} causes Joule heating.=

Owing to the low thermal conductivity of Bi_2O_2Se (~ 1.2 W/mK) [54,55] in comparison with the TE CuO//Cu (33 W/mK//400 W/mK) and PdO//Pd (20 W/mK//71.2 W/mK), maximum thermal heat dissipation occurs at the CuO/Bi_2O_2Se interface and Bi_2O_2-Se/PdO interface through Bi_2O_2Se (SM).

Therefore, weak CF dissolution occurs in Bi_2O_2Se, while residual CFs remain at the CuOx/Bi_2O_2Se and Bi_2O_2Se/PdOx interfaces, supporting the repeatable switching. Furthermore, these nonlasting residual CFs play a crucial role in endurance and long uniform retention characteristics.

Since the Bi_2O_2Se-based structure has successfully emulated the synaptic characteristics of LTP and LTD, it is worthwhile to elucidate the mechanism involved in such performance. The proposed mechanism for synaptic emulation is based on the formation and rupture of CFs in a controlled manner via the application of voltage pulses of requisite amplitude and polarity. The device under the RESET condition was used to mimic synaptic characteristics. Fig. 5-d explains the mechanism of the application of positive voltage pulses on the TE. Cu atoms are oxidized to Cu^{z+} ions, which are reduced to Cu atoms at the BE, and their accumulation forms a CF of low thickness, attaining moderate conductance representing STP. When the positive voltage pulses are increased to an adequate number, the thickness of the CF increases, leading to an enhancement in the conductance, resulting in LTP, as shown in Fig. 5-e. In synapses, depression is considered the reverse action of potentiation, meaning a reduction in conductance via rupturing of the CF by applying voltage pulses of opposite polarity on the TE. Upon the application of a small number of negative voltage pulses, the CF (of Cu atoms) is supposed to be slightly dissolved, causing the conductance to start decreasing, representing STD, as shown in Fig. 5-f. By increasing the number of similar negative voltage pulses, the dissolution of the CF becomes crucial for lowering the conductance, emulating LTD, as shown in Fig. 5-g. Therefore, the Bi_2O_2Se-based device can be considered a typical artificial synaptic device because it emulates LTP and LTD behavior via controlled formation and dissolution of CFs, respectively. The performance (memory and artificial synapse) of the Bi_2O_2Se-based CBRAM device is compared with that of devices in recent reported references, as presented in Table 1 [23,56–59].

The comparison is focused on the major performance parameters, including the compliance current (CC), ON/OFF ratio, retention, P/E endurance, and artificial synaptic activities.

The compliance current (CC) for our device is 1 mA, a value in agreement with previous reports [56–58]. The ON/OFF ratio measured is > 10, an average acceptable value compared with references [23,59]. The device presents retention for over 10 ks, which is a reasonable value [56–58]. Multilevel switching, an advanced memory function that is not commonly reported [59], was investigated with the present device via four distinct read levels (Vread = 0.1, 0.2, 0.25, 0.3 V). The P/E endurance measured is $> 3.5 \times 10^3$ with a pulse width of 100 ns and applied voltage levels of 1.0/-0.8 V. The numbers of LTP (54, 0.3 V) and LTD (105, −0.6 V) states are also comparable with those in references crucially reporting artificial synapse activities [23,57–59]. Although the performance of the Bi_2O_2Se-based CBRAM device (studied for the first time) shows competitiveness for many parameters, further investigations are needed for performance improvement.

3.5. Cu migration analysis via HRTEM

To validate the proposed switching mechanism via well-controlled migration of Cu through the SM Bi_2O_2Se, ex situ high-resolution transmission electron microscopy (HRTEM) analysis was performed to achieve a visual view supporting the mechanism of the Bi_2O_2Se-based CBRAM device. Before HRTEM analysis, all the measurements were completed with the device kept in the SET condition. Fig. 6a presents a schematic diagram of the proposed Bi_2O_2Se-based CBRAM structure. The successfully fabricated structure is shown in Fig. 6b. Fig. 6c shows an HRTEM image of the major portion of the fabricated Cu/Bi_2O_2Se(SM)/Pd structure. The TE Cu is partially oxidized and forms CuOx at the Cu/Bi_2O_2Se interface, transforming the top layer from Cu to Cu/CuOx. Additionally, the interface of the BE also shows a thin layer of oxidized Pd, which is converted into PdOx/Pd at the Bi_2O_2Se/Pd interface. The approximate thicknesses of the CuOx, Bi_2O_2Se, and PdOx layers are 4 nm, 25 nm, and 3.5 nm, respectively. The presence of the layered structured

Table-1
Performance comparison of CBRAM with that of devices in recent reported references.

	Memory Performance							Artificial Synapse		
Device Structure	CC (μA)	HRS/LRS (ratio)	Retention (s)	Multilevel RS (levels)	P/E (V)	P/E pulse width (ns)	P/E endurance (#)	LTP/LTD states	LTP/ LTD (V)	Ref
Al/Cu/Bi_2O_2Se/Pd	10^3	>10	10^4	4	1.0/-0.8	100	$>3.5 \times 10^3$	54/105	0.3/-0.6	This work
Ag/GeSe/Pt/Ti/SiO_2	5×10^3	<10	$>10^4$	~6	0.5/-0.5	3×10^3	$\sim 10^4$	~50/50	0.3/-0.5	[55]
Al/Cu/TiOx/MoS_2/TiN	200	10^2	10^4	–	1.2/-0.9	100	2×10^9	55/500	0.45/-0.45	[54]
Cu/AlOx/aCOx/TiNxOy/TiN	300–10^3	37	10^4	–	1.2/-0.8	100	1.5×10^9	59/101	0.5/-0.4	[53]
Cu/MoS_2 double-layer/Au	2×10^3	<10	18×10^3	–	–	–	–	20/20	0.6/-0.6	[21]
Cu/MoS_2/Ni–Mn–In	10^4	300	10^3	–	1.5/-1.5	100	500	–	–	[52]

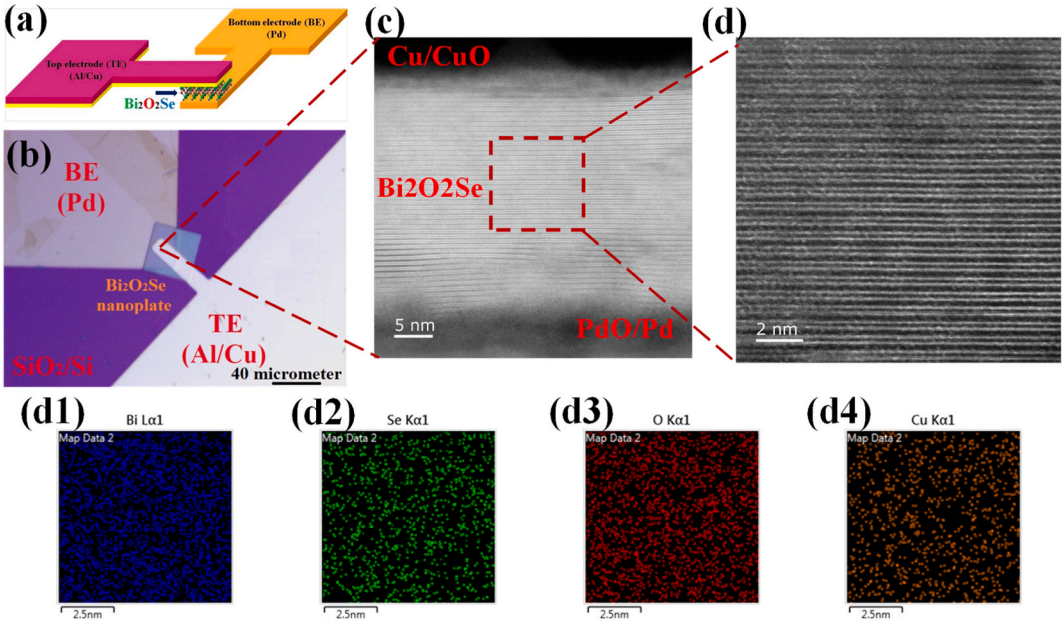

Fig. 6. High-resolution TEM analysis. (a) Proposed cross point structure. (b) Fabricated Bi_2O_2Se-based CBRAM device. (c) HRTEM image of a cross-sectional view of the device. (d) Layered structure of Bi2O2Se used as an SM. EDS elemental mapping of the switching region for "Bi", "Se", "O", and "Cu" (d1-4).

Bi_2O_2Se can be clearly observed, with a number of layers of ~42 (corresponding to a total thickness of ~25 nm) [39]. Fig. 6d shows an HRTEM image of an arbitrarily selected region of the SM, which presents the crystalline structure of Bi_2O_2Se with a clear view of distinct layers. Some part of the layered crystalline view exhibits black spots owing to the presence of Cu in the SM Bi_2O_2Se. To confirm the presence of Cu in the SM, energy dispersive spectroscopy (EDS) was carried out to map the elements. Fig. 6d (1–4) presents EDS elemental mapping images with differentiating colors for "Bi", "Se", "O", and "Cu". With the aid of this evidence, it is clear that the switching property of the fabricated device is due to Cu migration via the crystalline layered structure of Bi_2O_2Se, which is proposed as the SM in the present memory structure.

4. Conclusions

An Al/Cu/Bi_2O_2Se/Pd-based cross point CBRAM device was successfully fabricated. The device exhibits resistive switching at a low voltage level (+1.5 V/-1.5 V) and basic memory functions, including endurance (>90 cycles), cumulative probability (~99 %), and retention (@ Vread of 0.1 V) over 10 ks (R_{HRS}/R_{LRS} >10). In addition, the device shows multilevel switching behavior via four distinct stable switching states. Artificial synapses are mimicked by conductivity modulation, showing potentiation (35 states) and depression (41 states). The current conduction mechanism encompasses Schottky (during the HRS) and Ohmic (during the LRS) conduction phenomena. Furthermore, the switching mechanism involving Cu migration through Bi_2O_2Se has been conceptually explained with the aid of HRTEM imaging. With our findings, Bi_2O_2Se-based CBRAM devices can potentially be applied for memory and artificial synapse applications.

Data availability statement

The data can be obtained from authors on reasonable request.

CRediT authorship contribution statement

Dharmendra Verma: Conceptualization, Data curation, Formal analysis, Investigation, Methodology, Validation, Visualization, Writing – original draft. **Tsung-Cheng Chen:** Formal analysis, Validation, Visualization, Writing – review & editing. **Bo Liu:** Formal analysis, Validation, Visualization, Writing – review & editing. **Chao-Sung Lai:** Conceptualization, Funding acquisition, Investigation, Project administration, Resources, Supervision, Validation, Visualization, Writing – review & editing.

Declaration of competing interest

The authors declare that they have no known competing financial interests or personal relationships that could have appeared to

influence the work reported in this paper.

Acknowledegment

The present study was financially supported by grants from the Ministry of Science and Technology (MOST), Taiwan (MOST 109-2221-E-182 -013 -MY3, MOST 110-2221-E-182 -043 -MY3, and MOST 111-2119-M-492-001 –MBK), and Chang Gung Memorial Hospital (CGMH), Taiwan with grant No. CORPD2J0073 and CMRPD2N0031.

Appendix A. Supplementary data

Supplementary data to this article can be found online at https://doi.org/10.1016/j.heliyon.2023.e22512.

References

[1] M.D. Tran, H. Kim, J.S. Kim, M.H. Doan, T.K. Chau, Q.A. Vu, J.H. Kim, Y.H. Lee, Two-terminal multibit optical memory via van der Waals heterostructure, Adv. Mater. 31 (2019), 1807075, https://doi.org/10.1002/adma.201807075.
[2] E. Chicca, F. Stefanini, C. Bartolozzi, G. Indiveri, Neuromorphic electronic circuits for building autonomous cognitive systems, Proc. IEEE 102 (2014) 1367, https://doi.org/10.1109/JPROC.2014.2313954.
[3] C. Chappert, A. Fert, F.N. Van Dau, The emergence of spin electronics in data storage, Nat. Mater. 6 (2007) 813, https://doi.org/10.1038/nmat2024.
[4] S. Raoux, W. Wełnic, D. Ielmini, Phase change materials and their application to nonvolatile memories, Chem. Rev. 110 (2010) 240–267, https://doi.org/10.1021/cr900040x.
[5] G. Zhou, B. Sun, X. Hu, L. Sun, Z. Zou, B. Xiao, W. Qiu, B. Wu, J. Li, J. Han, L. Liao, C. Xu, G. Xiao, L. Xiao, J. Cheng, S. Zheng, L. Wang, Q. Song, S. Duan, Negative photoconductance effect: an extension function of the TiO_x-based memristor, Adv. Sci. 8 (2021), 2003765, https://doi.org/10.1002/advs.202003765.
[6] Y. Xue, Y. Cheng, Y. Zheng, S. Yan, W. Song, S. Lv, S. Song, Z. Song, Phase change memory based on Ta-Sb-Te alloy towards a universal memory, Materials Today Physics 15 (2020), 100266, https://doi.org/10.1016/j.mtphys.2020.100266.
[7] J. Rao, Z. Fan, L. Hong, S. Cheng, Q. Huang, J. Zhao, X. Xiang, E.J. Guo, H. Guo, Z. Hou, Y. Chen, X. Lu, G. Zhou, X. Gao, J.M. Liu, An electroforming-free, analog interface-type memristor based on a SrFeOx epitaxial heterojunction for neuromorphic computing, Materials Today Physics 18 (2021), 100392, https://doi.org/10.1016/j.mtphys.2021.100392.
[8] B. Sun, G. Zhou, T. Guo, Y.N. Zhou, Y.A. Wu, Biomemristors as the next generation bioelectronics, Nano Energy 75 (2020), 104938, https://doi.org/10.1016/j.nanoen.2020.104938.
[9] T.C. Chang, K.C. Chang, T.M. Tsai, T.J. Chu, S.M. Sze, Resistance random access memory, Mater. Today 19 (2016) 254–264, https://doi.org/10.1016/j.mattod.2015.11.009.
[10] D.B. Strukov, G.S. Snider, D.R. Stewart, R.S. Williams, The missing memristor found, Nature 453 (2008) 80–83, https://doi.org/10.1038/nature06932.
[11] K. Yan, M. Peng, X. Yu, X. Cai, S. Chen, H. Hu, B. Chen, X. Gao, B. Dong, D. Zou, High-performance perovskite memristor based on methyl ammonium lead halides, J. Mater. Chem. C 4 (2016) 1375–1381, https://doi.org/10.1039/C6TC00141F.
[12] M.J. Lee, C.B. Lee, D. Lee, S.R. Lee, M. Chang, J.H. Hur, Y.B. Kim, C.J. Kim, D.H. Seo, S. Seo, U.I. Chung, I.K. Yoo, K. Kim, A fast, high-endurance and scalable non-volatile memory device made from asymmetric Ta_2O_{5-X}/TaO_{2-X} bilayer structures, Nat. Mater. 10 (2011) 625–630, https://doi.org/10.1038/nmat3070.
[13] Y. Yang, J. Ouyang, L. Ma, R.J.H. Tseng, C.W. Chu, Electrical switching and bistability in organic/polymeric thin films and memory devices, Adv. Funct. Mater. 16 (2006) 1001–1014, https://doi.org/10.1002/adfm.200500429.
[14] J. Tang, F. Yuan, X. Shen, Z. Wang, M. Rao, Y. He, Y. Sun, X. Li, W. Zhang, Y. Li, Adv. Mater, Bridging Biological and Artificial Neural Networks with Emerging Neuromorphic Devices: Fundamentals, Progress, and Challenges 31 (2019), 1902761, https://doi.org/10.1002/adma.201902761.
[15] Q. Xia, J.J. Yang, Memristive crossbar arrays for brain-inspired computing, Nat. Mater. 18 (2019) 309–323, https://doi.org/10.1038/s41563-019-0291-x.
[16] Z. Wang, H. Wu, G.W. Burr, C.S. Hwang, K.L. Wang, Q. Xia, J.J. Yang, Resistive switching materials for information processing, Nat. Rev. Mater. 5 (2020) 173–195, https://doi.org/10.1038/s41578-019-0159-3.
[17] M. Lanza, H.S.P. Wong, E. Pop, D. Ielmini, D. Strukov, B.C. Regan, L. Larcher, M.A. Villena, J.J. Yang, L. Goux, A. Belmonte, Y. Yang, F.M. Puglisi, J. Kang, B. M. Köpe, E. Yalon, A. Kenyon, M. Buckwell, A. Mehonic, A. Shluger, H. Li, T.H. Hou, B. Hudec, D. Akinwande, R. Ge, S. Ambrogio, J.B. Roldan, E. Miranda, J. Sune, K.L. Pey, X. Wu, N. Raghavan, E. Wu, W.D. Lu, G. Navarro, W. Zhang, H. Wu, R. Li, A. Holleitner, U. Wurstbauer, M.C. Lemme, M. Liu, S. Long, Q. Liu, H. Lv, A. Padovani, P. Pavan, I. Valov, X. Jing, T. Han, K. Zhu, S. Chen, F. Hui, Y. Shi, Recommended methods to study resistive switching devices, Adv. Electron. Mater. 5 (2019), 1800143, https://doi.org/10.1002/aelm.201800143.
[18] J.R. Jameson, N. Gilbert, F. Koushan, J. Saenz, J. Wang, S. Hollmer, M. Kozicki, N. Derhacobian, Quantized conductance in $Ag/GeS_2/W$ conductive-bridge memory cells, IEEE Electron. Device Lett. 33 (2012) 257–259, https://doi.org/10.1109/LED.2011.2177803.
[19] S. Tappertzhofen, H. Mündelein, I. Valov, R. Waser, Nanoionic transport and electrochemical reactions in resistively switching silicon dioxide, Nanoscale 4 (2012) 3040–3043, https://doi.org/10.1039/C2NR30413A.
[20] K. Krishnan, M. Muruganathan, T. Tsuruoka, H. Mizuta, M. Aono, Highly reproducible and regulated conductance quantization in a polymer-based atomic switch, Adv. Funct. Mater. 27 (2017), 1605104, https://doi.org/10.1002/adfm.201605104.
[21] S.L. Patil, O.Y. Pawar, H.S. Patil, S.S. Sutar, G.U. Kamble, Deok-kee Kim, J.H. Kim, T.G. Kim, R.K. Kamat, T.D. Dongale, N.L. Tarwal, The $g\text{-}C_3N_4\text{-}TiO_2$ nanocomposite for non-volatile memory and artificial synaptic device applications, J. Alloys Compd. 962 (2023), 171024, https://doi.org/10.1016/j.jallcom.2023.171024.
[22] S.L. Patil, R.S. Redekar, O.Y. Pawar, S.S. Kundale, S.S. Sutar, K.V. More, V.D. Chavan, Deok-kee Kim, T.D. Dongale, N.L. Tarwal, Precursor-dependent resistive switching properties of nanostructured $g\text{-}C_3N_4$: statistical and experimental investigations, J. Mater. Sci. Mater. Electron. 34 (2023) 155, https://doi.org/10.1007/s10854-022-09436-7.
[23] R. Xu, H. Jang, M.H. Lee, D. Amanov, Y. Cho, H. Kim, S. Park, H.J. Shin, D. Ham, Vertical MoS_2 double-layer memristor with electrochemical metallization as an atomic-scale synapse with switching thresholds approaching 100 mV, Nano Lett. 19 (2019) 2411–2417, https://doi.org/10.1021/acs.nanolett.8b05140.
[24] R. Tripathi, P. Bhattacharyya, S. Nandi, A. Shukla, A. Misra, Molecular switching operation in gate constricted interface of MoS_2 and hBN heterostructure, Appl. Mater. Today 23 (2021), 100999, https://doi.org/10.1016/j.apmt.2021.100999.
[25] Y. Shi, X. Liang, B. Yuan, V. Chen, H. Li, F. Hui, Z. Yu, F. Yuan, E. Pop, H.S.P. Wong, Electronic synapses made of layered two-dimensional materials, Nat. Electron. 1 (2018) 458–465, https://doi.org/10.1038/s41928-018-0118-9.
[26] S. Rehman, M.F. Khan, S. Aftab, H. Kim, J. Eom, D.K. Kim, Thickness-dependent resistive switching in black phosphorus CBRAM, J. Mater. Chem. C 7 (2019) 725–732, https://doi.org/10.1039/C8TC04538K.
[27] K.A. Nirmal, W. Ren, A.C. Khot, D.Y. Kang, T.D. Dongale, T.G. Kim, Flexible memristive organic solar cell using multilayer 2D titanium carbide MXene electrodes, Adv. Sci. 10 (2023), 2300433, https://doi.org/10.1002/advs.202300433.

[28] J. Wu, H. Yuan, M. Meng, C. Chen, Y. Sun, Z. Chen, W. Dang, C. Tan, Y. Liu, J. Yin, Y. Zhou, S. Huang, H.Q. Xu, Y. Cui, H.Y. Hwang, Z. Liu, Y. Chen, B. Yan, H. Peng, High electron mobility and quantum oscillations in non-encapsulated ultrathin semiconducting Bi_2O_2Se, Nat. Nanotechnol. 12 (2017) 530–534, https://doi.org/10.1038/nnano.2017.43.

[29] X. Ma, D. Chang, C. Zhao, R. Li, X. Huang, Z. Zeng, X. Huang, Y. Jia, Geometric structures and electronic properties of the Bi_2X_2Y (X, Y = O, S, Se, and Te) ternary compound family: a systematic DFT study, J. Mater. Chem. C 48 (2018) 13241–13249, https://doi.org/10.1039/C8TC04587A.

[30] Y.D. Xu, C. Wang, Y.Y. Lv, Y.B. Chen, S.H. Yao, J. Zhou, Infrared and Raman spectra of Bi_2O_2X and Bi_2OX_2 (X = S, Se, and Te) studied from first principles calculations, RSC Adv. 31 (2019) 18042–18049, https://doi.org/10.1039/C9RA02584G.

[31] J. Wu, C. Tan, Z. Tan, Y. Liu, J. Yin, W. Dang, M. Wang, H. Peng, Controlled synthesis of high mobility atomically thin bismuth oxyselenide crystals, Nano Lett. 17 (2017) 3021–3026, https://doi.org/10.1021/acs.nanolett.7b00335.

[32] S.L. Li, K. Tsukagoshi, E. Orgiu, P. Samori, Charge transport and mobility engineering in two-dimensional transition metal chalcogenide semiconductors, Chem. Soc. Rev. 45 (2016) 118–151, https://doi.org/10.1039/C5CS00517E.

[33] K.A. Kokh, N.A. Nebogatikova, I.V. Antonova, D.A. Kustov, V.A. Golyashov, E.S. Goldyreva, N.P. Stepina, V.V. Kirienko, O.E. Tereshchenko, Vapor growth of Bi_2Se_3 and Bi_2O_2Se crystals on mica, Mater. Res. Bull. 129 (2020), 110906, https://doi.org/10.1016/j.materresbull.2020.110906.

[34] W. Zhang, Z. Huang, W. Zhang, Y. Li, Two-dimensional semiconductors with possible high room temperature mobility, Nano Res. 12 (2014) 1731–1737, https://doi.org/10.1007/s12274-014-0532-x.

[35] T. Ghosh, M. Samanta, A. Vasdev, K. Dolui, J. Ghatak, T. Das, G. Sheet, K. Biswas, Ultrathin free-standing nanosheets of Bi_2O_2Se: room temperature ferroelectricity in self-assembled charged layered heterostructure, Nano Lett. 19 (2019) 5703–5709, https://doi.org/10.1021/acs.nanolett.9b02312.

[36] M.Q. Li, L.Y. Dang, G.G. Wang, F. Li, M. Han, Z.P. Wu, G.Z. Li, Z. Liu, J.C. Han, Bismuth oxychalcogenide nanosheet: facile synthesis, characterization, and photodetector application, Adv. Mater. Technol. 5 (2020), 2000180, https://doi.org/10.1002/admt.202000180.

[37] Z. Lin, Y. Liu, U. Halim, M. Ding, Y. Liu, Y. Wang, C. Jia, P. Chen, X. Duan, C. Wang, F. Song, M. Li, C. Wan, Y. Huang, X. Duan, Solution-processable 2D semiconductors for high-performance large-area electronics, Nature 562 (2018) 254–258, https://doi.org/10.1038/s41586-018-0574-4.

[38] P. Ruleov, C. Drasar, P. Lostak, C.P. Li, S. Ballikaya, C. Uher, Thermoelectric properties of Bi_2O_2Se, Mater. Chem. Phys. 119 (2010) 299–302, https://doi.org/10.1016/j.matchemphys.2009.08.067.

[39] U. Khan, Y. Luo, L. Tang, C. Teng, J. Liu, B. Liu, H.M. Cheng, Controlled vapor-solid deposition of millimeter-size single crystal 2D Bi_2O_2Se for high performance phototransistors, Adv. Funct. Mater. 29 (2019), 1807979, https://doi.org/10.1002/adfm.201807979.

[40] J. Yang, R. Quhe, Q. Li, S. Liu, L. Xu, Y. Pan, H. Zhang, X. Zhang, J. Li, J. Yan, B. Shi, H. Pang, L. Xu, Z. Zhang, J. Lu, J. Yang, Sub 10 nm bilayer Bi_2O_2Se transistors, Adv. Electron. Mater. 5 (2019), 1800720, https://doi.org/10.1002/aelm.201800720.

[41] R. Quhe, J. Liu, J. Wu, J. Yang, Y. Wang, Q. Li, T. Li, Y. Guo, J. Yang, H. Peng, M. Lei, J. Lu, High-performance sub-10 nm monolayer Bi_2O_2Se transistors, Nanoscale 11 (2019) 532–540, https://doi.org/10.1039/C8NR08852G.

[42] H. Yang, W. Chen, X. Zheng, D. Yang, Y. Hu, X. Zhang, X. Ye, Y. Zhang, T. Jiang, G. Peng, X. Zhang, R. Zhang, C. Deng, S. Qin, Near-infrared photoelectric properties of multilayer Bi_2O_2Se nanofilms, Nanoscale Res. Lett. 14 (2019) 371, https://doi.org/10.1186/s11671-019-3179-4.

[43] J. Li, Z. Wang, Y. Wen, J. Chu, L. Yin, R. Cheng, L. Lei, P. He, C. Jiang, L. Feng, J. He, High-performance near-infrared photodetector based on ultrathin Bi_2O_2Se nanosheets, Adv. Funct. Mater. 28 (2018), 1706437, https://doi.org/10.1002/adfm.201706437.

[44] Z. Zhang, T. Li, Y. Wu, Y. Jia, C. Tan, X. Xu, G. Wang, J. Lv, W. Zhang, Y. He, J. Pei, C. Ma, G. Li, H. Xu, L. Shi, H. Peng, H. Li, Truly concomitant and independently expressed short- and long-term plasticity in a Bi_2O_2Se-based three-terminal memristor, Adv. Mater. 31 (2019), 1805769, https://doi.org/10.1002/adma.201805769.

[45] C.M. Yang, T.C. Chen, D. Verma, L.J. Li, B. Liu, W.H. Chang, C.S. Lai, Bidirectional all-optical synapses based on a 2D Bi_2O_2Se/graphene hybrid structure for multifunctional optoelectronics, Adv. Funct. Mater. 30 (2020), 2001598, https://doi.org/10.1002/adfm.202001598.

[46] D. Verma, B. Liu, T.C. Chen, L.J. Li, C.S. Lai, Bi_2O_2Se-based integrated multifunctional optoelectronics, Nanoscale Adv. 4 (2022) 3832, https://doi.org/10.1039/d2na00245k.

[47] R. Xu, S. Wang, Y. Li, H. Chen, T. Tong, Y. Cai, Y. Meng, Z. Zhang, X. Wang, F. Wang, Layered semiconductor Bi_2O_2Se for broadband pulse generation in the near-infrared, IEEE Photon Technol. Lett. 31 (2019) 1056–1059, https://doi.org/10.1109/LPT.2019.2917472.

[48] B. Liu, Y. Zhao, D. Verma, L.A. Wang, H. Liang, H. Zhu, L.J. Li, T.H. Hou, C.S. Lai, Bi_2O_2Se-Based Memristor-Aided Logic, ACS Appl. Mater. Interfaces 13 (2021) 15391–15398, https://doi.org/10.1021/acsami.1c00177.

[49] W. Chen, R. Zhang, R. Zheng, B. Liu, Out-of-Plane resistance switching of 2D Bi_2O_2Se at the nanoscale, Adv. Funct. Mater. 31 (2021), 2105795, https://doi.org/10.1002/adfm.202105795.

[50] B. Liu, Y.F. Chang, J. Li, X. Liu, L.A. Wang, D. Verma, H. Liang, H. Zhu, Y. Zhao, L.J. Li, T.H. Hou, C.S. Lai, Bi_2O_2Se-Based True Random Number Generator for Security Applications, ACS Nano 16 (2022) 6847–6857, https://doi.org/10.1021/acsnano.2c01784.

[51] C.S. Lai, I. Chakraborty, H.H. Tai, D. Verma, K.P. Chang, J.C. Wang, Advanced impacts of nanotechnology and intelligence, IEEE Nanotechnology Magazine 17 (2023) 13–21, https://doi.org/10.1109/MNANO.2022.3228154.

[52] S.M. Sze, Physics of Semiconductor Devices, second ed., Wiley, Hoboken, New Jersey, 1981, pp. 1–880.

[53] H. Patil, H. Kim, K.D. Kadam, S. Rehman, S.A. Patil, J. Aziz, T.D. Dongale, Z.A. Sheikh, M.K. Rahmani, M.F. Khan, Deok-kee Kim, Flexible Organic−Inorganic halide perovskite-based diffusive memristor for artificial nociceptors, ACS Appl. Mater. Interfaces 15 (2023) 13238–13248, https://doi.org/10.1021/acsami.2c16481.

[54] X. Ding, M. Li, P. Chen, Y. Zhao, M. Zhao, H. Leng, Y. Wang, S. Ali, F. Raziq, X. Wu, H. Xiao, X. Zu, Q. Wang, A. Vinu, J. Yi, L. Qiao, Bi_2O_2Se: A rising star for semiconductor devices, Matter 5 (2022) 4274–4314, https://doi.org/10.1016/j.matt.2022.11.005.

[55] K. Zhang, C. Hua, X. Kang, S. Wang, Y. Xi, H. Liu, Synthesis and thermoelectric properties of Bi_2O_2Se nanosheets, Mater. Res. Bull. 48 (2013) 3968–3972, https://doi.org/10.1016/j.materresbull.2013.06.013.

[56] A. Kumar, S. Pawar, S. Sharma, D. Kaura, Bipolar resistive switching behavior in MoS_2 nanosheets fabricated on ferromagnetic shape memory alloy, Appl. Phys. Lett. 112 (2018), 262106, https://doi.org/10.1063/1.5037139.

[57] S. Ginnaram, J.T. Qiu, S. Maikap, Controlling Cu migration on resistive switching, artificial synapse, and glucose/saliva detection by using an optimized AlOx interfacial layer in a-COx-based conductive bridge random access memory, ACS Omega 5 (2020) 7032–7043, https://doi.org/10.1021/acsomega.0c00795.

[58] S. Ginnaram, S. Maikap, Memristive and artificial synapse performance by using $TiOx/Al_2O_3$ interface engineering in MoS_2-based metallic filament memory, J. Phys. Chem. Solid. 151 (2021), 109901, https://doi.org/10.1016/j.jpcs.2020.109901.

[59] A. Ali, H. Abbas, M. Hussain, S.H.A. Jaffery, S. Hussain, C. Choi, J. Jung, Thickness-dependent monochalcogenide GeSe-based CBRAM for memory and artificial electronic synapses, Nano Res. 15 (2022) 2263–2277, https://doi.org/10.1007/s12274-021-3793-1.